Sub-Microsecond-Resolved Multi-Speckle X-Ray Photon Correlation Spectroscopy with a Pixel Array Detector

Qingteng Zhang (张庆腾),[a] Eric M. Dufresne,[a] Suresh Narayanan,[a] Piotr Maj,[b] Anna Koziol,[b] Robert Szczygiel,[b] Pawel Grybos,[b] Mark Sutton[c] and Alec R. Sandy [a]*

[a]X-Ray Science Division, Argonne National Laboratory, 9700 South Cass Ave., Lemont IL 60439 USA, [b]AGH University of Science and Technology, av. Mickiewicza 30, Krakow 30-059, Poland, and [c]Department of Physics, McGill University, 3600 Rue University, Montréal QC H3A 2T8, Canada. E-mail: asandy@anl.gov

Abstract

We performed small-angle x-ray photon correlation spectroscopy (XPCS) measurements spanning delay times from 826 ns to 52.8 s using a photon-counting pixel array detector with a dynamic range of 0–3 (2 bits). The fine resolution and wide dynamic range of time scales was achieved by combining two modes of operation of the detector: i) continuous mode, where data acquisition and data readout are performed in parallel with a frame acquisition time of 19.36 μs, and ii) burst mode where 12 frames are acquired with frame integration times of either 2.56 μs/frame or 826 ns/frame followed by 3.49 ms or 1.16 ms, respectively, for readout. We demonstrated the applicability of the detector for performing multi-speckle XPCS by measuring the Brownian dynamics of 10-nm-radius gold and 57-nm-radius silica colloids in water at room temperature. In addition, we examined the capability of the detector to faithfully record

1- and 2-photon counts by comparing the statistical distribution of photon counts with expected probabilities from the negative binomial distribution. We find that in burst mode the ratio of 2s to 1s is markedly smaller than predicted and show that this is attributable to pixel-response dead-time.

1. Introduction

The implementation of multi-bend achromat (MBA) lattices in new and existing synchrotron-based x-ray sources [i.e., Eriksson *et al.* (2014)] will provide large increases in time-average coherent flux and promises even more dramatic gains in the time resolution of XPCS measurements since minimum accessible delay times scale with the square of the coherent flux (Jakeman, 1973; Falus *et al.*, 2006). To achieve the promised gains in time resolution, however, corresponding developments are required in high-speed, high-fidelity XPCS-relevant area detectors. For XPCS, area detectors have demonstrated considerable gains over point detectors because they span a range of reciprocal space enabling so-called multi-speckle XPCS with improved signal-to-noise ratios (SNR) for the same radiation dose (Dierker *et al.*, 1995; Lumma *et al.*, 2000; Falus *et al.*, 2006; Leitner *et al.*, 2009; Vodnala *et al.*, 2018; Verwohlt *et al.*, 2018), direction-sensitive studies (Livet *et al.*, 2006; Fluerasu *et al.*, 2008; Burghardt *et al.*, 2012; Shinohara *et al.*, 2013; Rogers *et al.*, 2014; Wandersman *et al.*, 2015; Nygård *et al.*, 2016; Lhermitte *et al.*, 2017) and the measurement of two-time correlation functions that provide information about intermittent dynamics and fluctuations away from equilibrium conditions (Malik *et al.*, 1998; Sutton *et al.*, 2003; Sanborn *et al.*, 2011; Müller *et al.*, 2011; Orsi *et al.*, 2012; Evenson *et al.*, 2015). In recent years, photon-counting pixel array detectors (PADs) have emerged as powerful tools for a number of x-ray-scattering techniques because of their ability to faithfully record wide dynamic range signals at synchrotrons, their absence

of readout noise and dark currents, their narrow point-spread response, large collection areas and relative ease of use, i.e., Broennimann *et al.* (2006) and Kraft *et al.* (2009). Such detectors have also found application in XPCS measurements because of their increasingly fast continuous frame rates and relatively small pixel sizes (Johnson *et al.*, 2012; Westermeier *et al.*, 2016; Zhang *et al.*, 2016). Comparing frame rates across different detectors, though an important metric for XPCS, is not so straightforward because of varying sensor sizes, bit depths and "continuous" acquisition times that often, in practice, require pauses for moving data from one location to another. Within these qualifiers, however, the fastest continuous frame rate for XPCS-suitable PADs is currently about 50 kHz (Zhang *et al.*, 2017). One way to significantly increase the frame rate is using a so-called burst mode that takes frames at very high speed by using memory local to a pixel to store a typically small number of frames before a slower readout. Several x-ray detectors using this mode of operation have been developed recently (Becker *et al.*, 2011; Becker *et al.*, 2013; Schwandt *et al.*, 2013; Philipp *et al.*, 2016). To date, these detectors are targeted towards x-ray free electron laser applications and have limited potential usefulness for XPCS at storage-ring-based light sources because of relatively large pixels and, more significantly, because the time scales provided during the burst, and the repeat between bursts, do not overlap yielding gaps in the desired continuous spectrum of XPCS delay times.

Here we present the use of the ultrafast x-ray camera (UFXC32k) (Grybos *et al.*, 2016; Koziol *et al.*, 2018) previously used for XPCS in a continuous measurement mode up to 50 kHz (Zhang *et al.*, 2017), in both burst and continuous modes to provide access to XPCS delay times from 826 ns to 52.8 s. In burst mode, the detector acquires 12 frames at one of two frame rates: 390 kHz (for 31 μs) or 1.2 MHz (for 9.9 μs). We demonstrate the applicability of this detector for XPCS by measuring the Brownian dynamics of 10-nm-radius gold and 57-nm-radius silica nanoparticles in

water. We also assess the ability of the detector to record scattered x-rays with high fidelity by analyzing the statistical distribution of 1- and 2-photon counts (1s and 2s) in a pixel within single frame exposure times, t_e, of 2.56 and 19.36 μs. We compare the measured distribution of counts to expectations for scattering with a partially coherent x-ray beam and find that for the burst-mode measurements, the ratio of 2s to 1s is significantly less than expected. We show that this difference is attributable to pixel-response dead-time, τ_D. The remainder of this paper is organized as follows: Sec. 2 summarizes the instrumentation, Sec. 3 discusses small-angle x-ray scattering (SAXS) and XPCS measurements made with the UFXC32k, Sec. 4 examines the distribution of photon counts recorded by the detector and Sec. 5 concludes.

2. Instrumentation

The UFXC32k detector is a dual-counter, photon-counting PAD comprised of 128×256 75-μm-square pixels. The sensor layer is silicon and is 320 μm thick. Technical details regarding the sensor design and the digitizing electronics have been published previously (Grybos *et al.*, 2016; Koziol & Maj, 2018). The detector control unit (DCU) is implemented using the National Instruments (NI) 7935 FlexRIO system equipped with the Kintex-7 xc7k410t FPGA, 2 GB of DRAM and a NI 6589 adapter module and was programmed using LabVIEW. The DCU implements both burst and continuous modes of operation; switching between modes is performed in software. To achieve the highest frame rates, the dynamic range is set to two bits (0–3) for both modes of operation. With 2-bit dynamic range, the frame rate in both continuous and burst modes depends only on the frequency of the clock signal sent to the detector by the DCU, so the faster the clock rate the faster the frame rate. For our measurements, the clock rate was set to 440 MHz in continuous mode and 310 MHz or 100 MHz in burst mode during 1.2 MHz or 390 kHz frame acquisition, respectively.

Another feature in the control system is data sparsification. Before the FPGA sends the frames accumulated inside DRAM memory to the DCU, it sparsifies the data. The sparsification algorithm sends only the addresses of pixels that were hit together with their counter values and the frame number in the data acquisition sequence. This approach produces smaller per-frame data sets allowing more frames to be collected before pausing and also makes the entire data acquisition pipeline faster than it would be otherwise. Lastly, we note that the continuous frame rate of nearly 52 kHz is considerably higher than the 11.8 kHz frame rate that was reported recently for the same detector system (Zhang *et al.*, 2016). The key feature that allowed the system to operate at higher frame rates in continuous mode was an upgrade of the DCU that now allows the digital communication to operate at considerably higher speeds.

In continuous mode, as illustrated in Fig. 1(a), the detector operates at a frame rate of 51.67 kHz—an exposure time of 19.36 μs—for the largest number of frames that can be accumulated in the DCU before acquisition is paused and the frames read out and transferred to a device with more storage. During this mode, each pixel is connected to two counters that are configured to alternately accumulate photon hits and then be read out largely eliminating exposure dead-time. I.e., during one 19.36 μs exposure, Counter 2 is accumulating x-ray counts while Counter 1 is read out within this period while in the next 19.36 μs exposure, Counter 1 is accumulating x-ray counts while Counter 2 is being read out and so on. The minimum delay time in this mode is the frame spacing of 19.36 μs while the longest delay time depends on a combination of the 2 GB of DRAM accessible by the FPGA and the signal level since the data is sparsified. For our measurement conditions this was a little over 3.87 s (200000).

In burst mode, as illustrated in Fig. 1(b), the detector acquires 12 frames and stores the counts in the two 14-bit counters that are integral to each pixel before a longer pause during which the frames stored in the counters are moved to the DCU. Following

this, the next burst is acquired. This process can be repeated until the DCU memory is filled and acquisition is paused for a longer period while the frames are transferred to another storage device. We tested this mode at two frame rates: the first, 390 kHz, provided an exposure time of 2.56 μs with a gap between bursts of 3.49 ms, while the second, 1.2 MHz, provided an exposure time of 826 ns with a gap between bursts of 1.16 ms. For the measurement conditions in this manuscript, the maximum number of frames acquired during either burst mode was 180,000. As illustrated in Fig. 1(b), the longest delay time achieved during a 390 kHz burst is $11 \times 2.56 = 28.16$ μs and this exceeds the shortest delay time in continuous mode. Moreover, the longest delay time achieved during a 1.2 MHz burst is $11 \times 0.826 = 9.1$ μs and this exceeds the shortest delay time in the 390 kHz burst mode. The combination of three exposure times using burst and continuous modes provides a gap-free measurement of delay times spanning 826 ns to 52.8 s. In the remainder of this document we refer to the combination of burst- and continuous-mode measurements as hybrid-mode measurements.

3. SAXS and XPCS

We evaluated the detector's ability to perform hybrid-mode XPCS measurements by making time-resolved coherent SAXS measurements, i.e., SA-XPCS measurements, at beamline 8-ID-I at the Advanced Photon Source (APS). The measurements were made in 324-bunch non-top-up mode operation of the storage ring. In this mode, the time between x-ray pulses is 11.4 ns, the bunch currents are uniform and they vary smoothly from 0.32–0.26 mA per bunch over the course of each 12-hour fill. One benefit of this mode is the uniform current per bunch that eliminates aliasing effects that could appear in burst-mode data from the uneven distribution of bunch currents during the APS's more typical 24-bunch top-up operation since the storage ring revolution time of 3.682 μs is longer than the burst-mode exposures of 826 ns

or 2.56 μs. A drawback is that the bunch separation is considerably less than the pixel-response dead time, τ_D, (Walko *et al.*, 2008) that we estimate is 130 ns (see below). As we will discuss later, τ_D affects the detector's ability to faithfully record two (or more) one-photon hits in a pixel in a frame and this issue, especially during burst exposures, noticeably impacts determination of the speckle-pattern contrast via statistical distribution methods (Hruszkewycz *et al.*, 2012; Inoue *et al.*, 2012; Li *et al.*, 2014; Verwohlt *et al.*, 2018). This issue, however, has a negligible effect on average intensity measurements or time-series XPCS measurements provided that the characteristic sample fluctuation times are long compared to τ_D and the per-pixel signal rates are well below $1/\tau_D$ (Schätzel, 1986); both of these conditions are satisfied for the measurements presented below (Figs. 2–5).

The x-ray-beam was generated by tandem 33-mm-period, 2.4-m-long undulators. A plane silicon mirror at a deflection angle of 5 mrad was used to filter out higher harmonics and a Ge(111) monochromator with a relative bandpass of 0.03% full-width-at-half-maximum (FWHM) selected a 10.91 keV x-ray beam. A 180 μm vertical portion of the incident beam (approximately the vertical coherence length at the position of the focusing optic) was focused 2 m downstream to a FWHM at the sample position of 2 μm using Be compound refractive lenses. In the horizontal direction, a 20 μm horizontal collimating slit selected a few horizontal coherence lengths of the incident beam. The partially coherent flux at the sample position was 3.8×10^{10} photons/s. Three guard slits between the beam-defining slits and the sample were used to reduce parasitic scattering. The detector was placed 4 m downstream of the sample and a tungsten beamstop immediately upstream of the detector blocked the transmitted direct beam.

We performed SA-XPCS measurements of citrate-capped spherical gold nanoparticles dispersed in water at a volume fraction of 0.026% and silica nanoparticles dispersed

in water at a volume fraction of 2.5%. All measurements were made at room temperature. For the gold nanoparticles, the sample was contained in a 1.5-mm-diameter quartz capillary. For the silica nanoparticles, the sample was sealed in an aluminum cell with Kapton windows for x-ray access. The sample thickness along the x-ray beam is 1.5 mm. Figure 2 shows the 2-D scattering from the gold nanoparticle sample: Fig. 2(a) is the time average of 20,000 frames collected in continuous mode (0.39 s of counting time) while Fig. 2(b) is the average of 180,000 frames collected in 2.56 μs burst mode (52.8 s = 0.46 s of counting time and 52.4 s of counter readout). The x and y axes are in units of Q where $Q = 2k\sin(2\theta/2)$ is the wave-vector transfer, $k = 2\pi/\lambda$ is the wavevector, λ is the x-ray wavelength and 2θ is the scattering angle.

Figure 3 shows the 1-D SAXS results for the gold and silica nanoparticle suspensions obtained by azimuthally averaging the 2-D scattering intensities like those shown in Fig. 2 around the origin of reciprocal space. The intensities are plotted versus scaled wavevector QR where R are the fitted radii of the different nanoparticle suspensions. Open and closed symbols are gold suspension continuous- and burst-mode data, respectively, while plus symbols are data from the silica suspension. The gold continuous-mode results were collected at 5 detector positions to span a larger range of reciprocal space but because of intensity limitations the XPCS analysis was confined to the smallest Q values shown by the green shaded rectangle in Fig. 3. The difference in intensities between the continuous- and burst-mode gold data is the ratio of exposure times while the intensities from the silica suspension are higher because of the larger particle size and concentration. The nanoparticle sizes can be estimated by fitting the data to a model comprised of spherical particles having a Gaussian size distribution (Rieker *et al.*, 1999). For gold, reasonable agreement is found between the experimental results and the form factor for spheres with a mean radius of 9.8 nm and a standard deviation of 0.8 nm (black dashed line). The discrepancy at smaller

Q likely arises from some aggregation of the gold nanoparticles which might have occurred because the sample was not measured for a long time after it was purchased from the vendor. For silica, the same analysis yields a mean nanoparticle radius of 56.8 nm and a standard deviation of 4.8 nm.

The Q-dependent intensity autocorrelation function, $g_2(Q,t)$, of the nanoparticle suspensions is calculated according to:

$$g_2(Q,t) = \frac{\langle\langle I_{i,j}(t') \cdot I_{i,j}(t'+t)\rangle_{t'}\rangle_{i,j}}{\langle\langle I_{i,j}(t')\rangle_{t'}\rangle_{i,j} \cdot \langle\langle I_{i,j}(t'+t)\rangle_{t'+t}\rangle_{i,j}} \tag{1}$$

where t is the delay time, $I_{i,j}(t')$ and $I_{i,j}(t+t')$ are the scattering intensities at pixel (i,j) collected at times t' and $t+t'$, respectively. As discussed previously (Wong & Wiltzius, 1993; Dierker et $al.$, 1995; Cipelletti & Weitz, 1999; Lumma et $al.$, 2000) and reflected in Eq. 1, the correlations (numerator) are computed on a pixel-by-pixel basis first and then can be averaged within annuli of nominally equivalent Q values to obtain improved signal. This approach also has the virtue of allowing the speckle contrast to be determined in a time series even if the sample is static (Lumma et $al.$, 2000). The correlations in the numerator are computed using the so-called multitau algorithm (Schätzel, 1990; Schätzel, 1993; Cipelletti & Weitz, 1999; Magatti & Ferri, 2001) yielding logarithmically spaced delay times. The averages in the denominator are calculated using smoothed symmetric normalization (Lumma et $al.$, 2000). The pixel averages $\langle...\rangle_{i,j}$ were performed over pixels that fall within a range of Q approximately one pixel wide (1.0×10^{-4} Å^{-1}) to eliminate the effect of intensity variations with Q on g_2. The $g_2(Q,t)$s are further binned by a factor of 10 in Q to improve the SNR with the error bars approximated by the standard deviation of the g_2s calculated for each pixel within each Q bin.

To calculate g_2 for data acquired in hybrid mode, up to five time scales must be managed. Burst-mode data provides 2.56-μs- and 3.52-ms-resolution (3.49 ms + 12 $\times$ 2.56 μs, solid diamonds in Figs. 4 and 5) and 826-ns- and 1.17-ms-resolution (1.16 ms

+ 12 × 0.826 μs, empty diamonds in Fig. 5) results and g_2 for data acquired in each of these modes is calculated using the framework developed for kinetics-mode area-detector XPCS data (Lumma *et al.*, 2000). Continuous-mode data provides 19.36-μs-resolution results (open circles in Figs. 4 and 5). The g_2s from the burst and continuous modes are merged to produce g_2s like those presented in Figs. 4 and 5.

Figure 4 shows $\Delta g_2 = g_2 - 1$ plotted versus the delay time for $Q = 0.0042$ Å^{-1}. The 2.56 μs burst-mode measurements contain 30,000 frames and were repeated 800× to improve the SNR while continuous-mode measurements contain 20,000 frames and were repeated 200×. The burst-mode results become increasingly noisy at larger delay times within each burst sequence because there are increasingly fewer intensity pairs to correlate. Nevertheless, there is good overlap with the continuous-mode data and for correlation function fitting we can exclude the noisiest burst-mode data and use just the continuous-mode data.

As shown by the fit result (black dashed line) in Fig. 4, $\Delta g_2(Q,t)$ is well-described using a Q-dependent exponential decay:

$$\Delta g_2(Q,t) = \beta_1 \exp\left(-2t/\tau(Q)\right), \tag{2}$$

where β_1 is the amplitude of the correlation function in the limit $t \to 0$ and reflects instrumental effects like the coherence of the beam relative to beamline aperture sizes and the pixel size of the detector, and $\tau(Q)$ is the Q-dependent correlation decay time. For simple diffusion anticipated for a dilute solution of spherical nanoparticles, $\tau(Q) = 1/(D_0 Q^2)$, with $D_0 = k_B T/(6\pi\eta R)$ the diffusion coefficient, k_B the Boltzmann constant, T the temperature, η the viscosity and R the particle radius. Open squares in the inset show the fitted values of τ versus Q and the solid line is a fit to this data with the slope fixed at -2. The slope was fixed to -2 since the Q-range of our measurements is not sufficient to enable more quantitative analysis (and because there is no reason to believe that the slope should not be -2 for the relatively dilute suspension that

we studied). Evidently, our results are consistent with the nanoparticles exhibiting simple Brownian diffusion. Given the evidence for aggregation seen at small Q in Fig. 3, we calculated the radius of gyration of the gold nanoparticle suspension from the fitted line using $\eta = 8.9 \times 10^{-4}$ Pa/s (the viscosity of water at room temperature) and find $R = 19.9$ nm. This is a factor of two larger than the SAXS results. In this same vein, we note that from the vendor, we know that the gold nanoparticles have a $\approx$ 2-nm-thick citrate capping layer (that is largely invisible to SAXS) so with regards to diffusion, even un-aggregated gold particles would have a hydrodynamic radius of 11.8 nm. Ultimately, these discrepancies reflect the fact that SAXS and XPCS are sensitive to different things: SAXS sees the size of the gold in the nanoparticles (and some aggregation of the gold) while XPCS sees the diffusion of the suspension which depends on the particle hydrodynamic radius and aggregation.

Figure 5 presents results like those discussed above but for the 57-nm-radius silica nanoparticles. The particles scatter more and the diffusion is slower so the quality of the measured correlation function is much higher. Both the 826 ns and 2.56 μs measurements contain 180,000 frames and were repeated 100$\times$ and 13$\times$, respectively, to improve the SNR while continuous-mode measurements contain 50,000 frames and were repeated 20$\times$. The inset to Fig. 5 shows the fitted results for $\tau(Q)$ (open squares) with a line of slope = -2 fitted to the points. The particle radius is determined as described above and yields $R = 64.8$ nm. This is 14% larger than the radius determined from SAXS.

As discussed above, the error bars on g_2 determined via the variance of g_2 within nominally equivalent Q bands and plotted in Figs. 4 and 5 are quite different because of the large difference in scattering signals among other factors. Under assumptions applicable to our measurements the expected SNR for a measurement of g_2 has pre-

viously been shown to be (Falus *et al.*, 2006):

$$\text{SNR}_{g_2} = \beta_1 \langle I \rangle t_e \sqrt{N_\text{f} N_\text{p}}. \tag{3}$$

$\langle I \rangle$ is the average count rate per pixel, t_e the exposure time, N_f the number of frames (measurement time), and N_p the number of pixels in the time and pixel averages in Eq. 1. It can be seen that the quality with which g_2 is measured can be improved, for example, by acquiring more frames (measuring longer) or with more coherent flux.

Equation 3 also demonstrates the power of multi-speckle XPCS since the SNR increases with square root of the number of equivalent measurements (pixels). Figure 6(a) shows the signal in a single frame from the 57-nm-radius silica suspension acquired during 1.2 MHz burst-mode operation. The grey circle is the masked-out shadow of the direct-beam stop, the dashed circles are the dynamic Q partitions and the red and green dots are pixels that registered 1- or 2-photon counts, respectively, in the frame. This figure emphasizes how sparse the acquired data is but because many signals are acquired in parallel, high quality correlation functions like those shown in Figs. 4 and 5 are obtained. For reference, Fig. 6(b) shows the number of pixels contributing to the static (open circles) and dynamic (solid squares) Q partitions as discussed relative to Eq. 1. Lastly, though the g_2 SNR can be improved by repeating and averaging the same measurement, Fig. 6(c) shows that even a single 826-ns burst sequence of 180,000 frames acquired from the 57-nm-radius silica suspension (0.15 s of signal measurement) yields g_2 with sufficient accuracy to distinguish the short-time amplitude of g_2 from the long-time baseline.

4. Photon Counts Distribution

The average count rates per pixel are low because of the combination of selecting only a partially coherent x-ray beam from a third generation synchrotron, the short

exposure times, and the relatively dilute suspensions of small particles. On the one hand, this means that a 2-bit counter per pixel is sufficient for our measurements. On the other hand, since such low numbers of photons are recorded, it is instructive to know how well the detector records small numbers of scattered photons. We evaluated the detector's capabilities in this regard by examining the distribution of photon counts recorded during exposure times for continuous and 2.56 μs burst-mode operations and comparing the observed distributions to expectations for scattering with a partially coherent x-ray beam.

The expected distribution of photon counts depends, for example, on the beam coherence, dynamics in the sample and the exposure time, and has been described previously for a variety of detectors and experiment configurations (Livet *et al.*, 2000; Gutt *et al.*, 2009; Hruszkewycz *et al.*, 2012; Li *et al.*, 2014; Wingert *et al.*, 2015; Verwohlt *et al.*, 2018). For a partially coherent beam, the probability for k photons to be recorded in a pixel when the average count rate per pixel is $\bar{k}$ is given by the negative binomial distribution (Hruszkewycz *et al.*, 2012):

$$P(k) = \frac{\Gamma(k+M)}{\Gamma(M)\Gamma(k+1)} \left(1 + \frac{M}{\bar{k}}\right)^{-k} \left(1 + \frac{\bar{k}}{M}\right)^{-M}, \qquad (4)$$

where M is the number of coherent modes and Γ is the gamma function. In the limit of large M the probability reduces to the Poisson distribution: $P(k) = \bar{k}^k e^{-\bar{k}}/k!$. Other factors that affect the measured distributions are pixel-response dead-time, which is the time for the pixel electronics to recover after counting a photon, and the fact that the UFXC32k is a counting detector so any two-photon scattering events from a single bunch into a single pixel will be recorded as a single count. The pixel-response dead time, τ_D, of the UFXC32k has previously been measured to be as low as $\tau_D = 85$ ns (Grybos *et al.*, 2016) with near linear response to incoming photon fluxes to $\approx 10^6$ photons/pixel/s. The maximum scattering signals in our measurements, around 10^4 photons/pixel/s, are well below this limit. Moreover, τ_D is much greater than the

bunch separation (11 ns) suggesting that the source effectively appears continuous and the bunch structure is not important. These suggest, at first glance, that pixel-response dead-time need not be considered further and this is true for measurements of the average intensity (see below). On the other hand, measuring the contrast in a speckle pattern via speckle visibility depends sensitively on the relative distribution of 1s and 2s recorded in the detector during each integration time. Specifically, in the limit of weak scattering, Hruszkewycz et $al.$ (2012) showed that:

$$\beta = \frac{2P(2)[1 - P(1)]}{P(1)^2} - 1,\tag{5}$$

with $P(i)$ the probability of i photons being recorded in a pixel during an exposure time.

Figure 7 shows the β values calculated using Eq. 5 from the measured distribution of 1s and 2s for 2.56 μs burst- (open diamonds) and continuous-mode (open circles) data as a function of Q. Two features are immediately apparent. First, the β values for continuous-mode are roughly comparable to the amplitude of Δg_2 (β_1 = dashed line) as one would expect since the exposure time of the detector is essentially fast enough to capture the short-time amplitude of g_2 (see Fig. 4). A more thorough comparison would require comparing β determined via this visibility approach with smeared values of β_1 determined via a time autocorrelation. Details of this type of analysis are available and have been performed elsewhere (Bandyopadhyay et $al.$, 2005; Li et $al.$, 2014; Seaberg et $al.$, 2017; Verwohlt et $al.$, 2018). We have not pursued this approach here because with the limited integration times currently available from the UFXC32k (826 ns and 2.56 and 19.36 μs) we will not learn new information about the sample dynamics beyond what is available from measuring g_2. Second, and more striking, the β values obtained in burst mode are negative indicating that the ratio of 2s relative to 1s is less than expected. This observation is made more evident in Fig. 8 that shows the measured probability of 1- and 2-photon occurrences (top and bottom panels,

respectively) as a function of the average intensity in a pixel. The solid and dashed lines show the expected probabilities for fully coherent ($M = 1$) and fully incoherent (Poisson) scattering, respectively. The measured probability of 2s is slightly below even that expected for the Poisson distribution.

We consider two origins for the relative lack of 2s: i) 2-photon hits from a single bunch being recorded as a 1-photon hit because the UFXC32k is a counting detector and ii) the pixel-response dead-time suppressing the registration of more than one hit (from different bunches) during an exposure. The probability of 2-photon events from a single bunch is proportional to $P(1)^2$. This probability is considerably smaller than the probability for two 1s from different bunches so not a significant factor. With respect to pixel-response dead-time, as illustrated schematically in the bottom portion of Fig. 1(b), a photon hit (bold magenta signal) will preclude a second photon hit being counted if the photon arrivals are separated by a time gap shorter than the pixel-response dead-time (signals in the dashed yellow boxes). This is a more important effect for burst-mode because the relative error arising from this, $2\tau_D/t_e$, (Zhou, 2008) is much bigger.

To test this idea, we examined how the burst-mode β-values (Fig. 7) would change for different τ_Ds. The solid diamonds in Fig. 7 are the β values determined from the burst-mode data if the number of 2s was increased to correct for $\tau_D = 130$ ns. Such a correction would result in a 10.2% increase in the number of 2s. The pixel-response dead-time for the UFXC32k has previously been measured to be as low as 85 ns but depending on details of how the detector has been configured, can be as high as 240 ns (Grybos et $al.$, 2016). The dead-time was not measured for the particular detector configuration that we used but based on our knowledge of the configuration we used and how similar and different it is to other configurations that have been tested, we estimate $\tau_D = 125$–150 ns which encompasses our value of 130 ns.

To conclude this section we note that the photon-distribution effects we have been discussing do not affect either the measurement of g_2 determined by a time series of intensities (Figs. 4 and 5) or precise measurements of the time-average scattered intensity (Figs. 2 and 3). With respect to measuring time correlation functions with high fidelity, we note that τ_D affects measurements only when the sampling time is comparable to τ_D or the per-pixel count rate is high and non-linearity occurs (Schätzel, 1986). In our study, the smallest sampling time is 6× larger than our estimate for τ_D (130 ns) and the highest count rate, 10^4 photons/pixel/s, is 100× smaller than where saturation non-linearity starts to occur (Grybos *et al.*, 2016). With respect to time-average intensity measurements, we note that the one-photon count rates are far less than where saturation non-linearity occurs while for two photons, the dead-time leads to a 10.2% $(2\tau_D/t_e)$ reduction in signal in the burst mode (and less in continuous mode). The contribution of 2s to the total intensity is less than 2% so the effect of τ_D on the total recorded intensity is 0.2% which is much smaller than the error bars in Fig. 3.

5. Conclusions

We have demonstrated greatly increased time resolution for multi-speckle XPCS by using the UFXC32k detector in a so-called hybrid mode that combines burst and continuous modes to achieve XPCS sampling times continuously spanning 826 ns to 52.8 s or nearly 8 decades in delay time. By combining the g_2s calculated from these modes, we have demonstrated sub-microsecond-resolved multi-speckle XPCS. We have also demonstrated the ability of the UFXC32k to faithfully record scattered x-rays at low count rates by comparing the probability of expected and measured photon counts and show that these results are consistent with g_2 measurements provided that pixel-response dead-time effects are included. On the one hand, our results demonstrate the

need for PADs with increasingly smaller values of τ_D. On the other hand, our results show that multi-speckle g_2 measurements continue to work well at very short delay times even at very low average signal levels. Our work makes progress toward a key requirement for fully utilizing anticipated MBA sources for XPCS, namely the need for XPCS-suitable area detectors to record scattered x-rays with high fidelity and at very high frame rates spanning a large dynamic range in time.

Acknowledgements

References

Bandyopadhyay, R., Gittings, A. S., Suh, S. S., Dixon, P. K. & Durian, D. J. (2005). *Rev. Sci. Instrum.* **76**, 093110.

Becker, J., Bianco, L., Dinapoli, R., Göttlicher, P., Graafsma, H., Greiffenberg, D., Gronewald, M., Henrich, B. H., Hirsemann, H., Jack, S., Klanner, R., Klyuev, A., Krüger, H., Lange, S., Marras, A., Mozzanica, A., Schmitt, B., Schwandt, J., Sheviakov, I., Shi, X., Trunk, U., Zimmer, M. & Zhang, J. (2013). *J. Instrum.* **8**, C01042.

Becker, J., Gutt, C. & Graafsma, H. (2011). *J. Instrum.* **6**, P11005.

Broennimann, C., Eikenberry, E. F., Henrich, B., Horisberger, R., Huelsen, G., Pohl, E., Schmitt, B., Schulze-Briese, C., Suzuki, M., Tomizaki, T., Toyokawa, H. & Wagner, A. (2006). *J. Synchrotron Radiat.* **13**, 120–130.

Burghardt, W. R., Sikorski, M., Sandy, A. R. & Narayanan, S. (2012). *Phys. Rev. E*, **85**, 021402.

Cipelletti, L. & Weitz, D. A. (1999). *Rev. Sci. Instrum.* **70**, 3214.

Dierker, S. B., Pindak, R., Fleming, R. M., Robinson, I. K. & Berman, L. (1995). *Phys. Rev. Lett.* **75**, 449–452.

Eriksson, M., van der Veen, J. F. & Quitmann, C. (2014). *J. Synchrotron Radiat.* **21**, 837–842.

Evenson, Z., Ruta, B., Hechler, S., Stolpe, M., Pineda, E., Gallino, I. & Busch, R. (2015). *Phys. Rev. Lett.* **115**, 175701.

Falus, P., Lurio, L. B. & Mochrie, S. G. J. (2006). *J. Synchrotron Radiat.* pp. 253–259.

Fluerasu, A., Moussaïd, A., Falus, P., Gleyzolle, H. & Madsen, A. (2008). *J. Synchrotron Radiat.* **15**, 378–384.

Grybos, P., Kmon, P., Maj, P. & Szczygiel, R. (2016). *IEEE T. Nucl. Sci.* **63**, 1155–1161.

Gutt, C., Stadler, L. M., Duri, A., Autenrieth, T., Leupold, O., Chushkin, Y. & Grubel, G. (2009). *Opt. Express*, **17**, 55–61.

Hruszkewycz, S. O., Sutton, M., Fuoss, P. H., Adams, B., Rosenkranz, S., Ludwig, K. F., J., Roseker, W., Fritz, D., Cammarata, M., Zhu, D., Lee, S., Lemke, H., Gutt, C., Robert, A., Grubel, G. & Stephenson, G. B. (2012). *Phys. Rev. Lett.* **109**, 185502.

Inoue, I., Shinohara, Y., Watanabe, A. & Amemiya, Y. (2012). *Opt. Express*, **20**, 26878–26887.

Jakeman, E. (1973). In *Photon Correlation and Light Beating Spectroscopy*, edited by H. Z. Cummins & E. R. Pike, pp. 75–149. New York: Plenum.

Johnson, I., Bergamaschi, A., Buitenhuis, J., Dinapoli, R., Greiffenberg, D., Henrich, B., Ikonen, T., Meier, G., Menzel, A., Mozzanica, A., Radicci, V., Satapathy, D. K., Schmitt, B. & Shi, X. (2012). *J. Synchrotron Radiat.* **19**, 1001–1005.

Koziol, A., Bordessoule, M., Ciavardini, A., Dawiec, A., Da Silva, P., Desjardins, K., Grybos, P., Kanoute, B., Laulhe, C., Maj, P., Menneglier, C., Mercere, P., Orsini, F. & Szczygiel, R. (2018). *J. Synchrotron Radiat.* **25**, 413.

Koziol, A. & Maj, P. (2018). *J. Instrum.* **13**, C02049.

Kraft, P., Bergamaschi, A., Broennimann, C., Dinapoli, R., Eikenberry, E. F., Henrich, B., Johnson, I., Mozzanica, A., Schlepütz, C. M., Willmott, P. R. & Schmitt, B. (2009). *J. Synchrotron Radiat.* **16**, 368–375.

Leitner, M., Sepiol, B., Stadler, L. M., Pfau, B. & Vogl, G. (2009). *Nat. Mater.* **8**, 717–720.

Lhermitte, J. R., Rogers, M. C., Manet, S. & Sutton, M. (2017). *Rev. Sci. Instrum.* **88**, 015112.

Li, L., Kwasniewski, P., Orsi, D., Wiegart, L., Cristofolini, L., Caronna, C. & Fluerasu, A. (2014). *J. Synchrotron Radiat.* **21**, 1288–1295.

Livet, F., Bley, F., Ehrburger-Dolle, F., Morfin, I., Geissler, E. & Sutton, M. (2006). *J. Synchrotron Radiat.* **13**, 453–458.

Livet, F., Bley, F., Mainville, J., Caudron, R., Mochrie, S. G. J., Geissler, E., Dolino, G., Abernathy, D., Grubel, G. & Sutton, M. (2000). *Nucl. Instrum. Meth. A*, **451**, 596–609.

Lumma, D., Lurio, L. B., Mochrie, S. G. J. & Sutton, M. (2000). *Rev. Sci. Instrum.* **71**, 3274–3289.

Magatti, D. & Ferri, F. (2001). *Appl. Opt.* **40**, 4011–4021.

Malik, A., Sandy, A. R., Lurio, L. B., Stephenson, G. B., Mochrie, S. G. J., McNulty, I. & Sutton, M. (1998). *Phys. Rev. Lett.* **81**, 5832–5835.

Müller, L., Waldorf, M., Gutt, C., Grübel, G., Madsen, A., Finlayson, T. R. & Klemradt, U. (2011). *Phys. Rev. Lett.* **107**, 105701.

Nygård, K., Buitenhuis, J., Kagias, M., Jefimovs, K., Zontone, F. & Chushkin, Y. (2016). *Phys. Rev. Lett.* **116**, 167801.

Orsi, D., Cristofolini, L., Baldi, G. & Madsen, A. (2012). *Phys. Rev. Lett.* **108**, 105701.

Philipp, H. T., Tate, M. W., Purohit, P., Shanks, K. S., Weiss, J. T. & Gruner, S. M. (2016). *J. Synchrotron Radiat.* **23**, 395–403.

Rieker, T., Hanprasopwattana, A., Datye, A. & Hubbard, P. (1999). *Langmuir*, **15**, 638–641.

Rogers, M. C., Chen, K., Andrzejewski, L., Narayanan, S., Ramakrishnan, S., Leheny, R. L. & Harden, J. L. (2014). *Phys. Rev. E*, **90**, 062310.

Sanborn, C., Ludwig, K. F., Rogers, M. C. & Sutton, M. (2011). *Phys. Rev. Lett.* **107**, 015702.

Schätzel, K. (1986). *Appl. Phys. B*, **41**(2), 95–102.

Schätzel, K. (1990). *Quantum Opt.* **2**, 287–305.

Schätzel, K. (1993). In *Dynamic light scattering: The method and some applications*, edited by W. Brown. Oxford: Clarendon Press.

Schwandt, J., Fretwurst, E., Klanner, R., Poehlsen, T. & Zhang, J. (2013). *Nucl. Instrum. Meth. A*, **731**, 252–254.

Seaberg, M. H., Holladay, B., Lee, J. C. T., Sikorski, M., Reid, A. H., Montoya, S. A., Dakovski, G. L., Koralek, J. D., Coslovich, G., Moeller, S., Schlotter, W. F., Streubel, R., Kevan, S. D., Fischer, P., Fullerton, E. E., Turner, J. L., Decker, F. J., Sinha, S. K., Roy, S. & Turner, J. J. (2017). *Phys. Rev. Lett.* **119**.

Shinohara, Y., Watanabe, A., Kishimoto, H. & Amemiya, Y. (2013). *J. Synchrotron Radiat.* **20**, 801–804.

Sutton, M., Laaziri, K., Livet, F. & Bley, F. (2003). *Opt. Express*, **11**, 2268–2277.

Verwohlt, J., Reiser, M., Randolph, L., Matic, A., Medina, L. A., Madsen, A., Sprung, M., Zozulya, A. & Gutt, C. (2018). *Phys. Rev. Lett.* **120**, 168001.

Vodnala, P., Karunaratne, N., Lurio, L., Thurston, G. M., Vega, M., Gaillard, E., Narayanan, S., Sandy, A., Zhang, Q., Dufresne, E. M., Foffi, G., Grybos, P., Kmon, P., Maj, P. & Szczygiel, R. (2018). *Phys. Rev. E*, **97**, 020601.

Walko, D. A., Arms, D. A. & Landahl, E. C. (2008). *J. Synchrotron Radiat.* **15**, 612–617.

Wandersman, E., Chushkin, Y., Dubois, E., Dupuis, V., Robert, A. & Perzynski, R. (2015). *Soft Matter*, **11**, 7165–7170.

Westermeier, F., Pennicard, D., Hirsemann, H., Wagner, U. H., Rau, C., Graafsma, H., Schall, P., Paul Lettinga, M. & Struth, B. (2016). *Soft Matter*, **12**, 171–180.

Wingert, J., Singer, A. & Shpyrko, O. G. (2015). *J. Synchrotron Radiat.* **22**, 1141–1146.

Wong, A. P. Y. & Wiltzius, P. (1993). *Rev. Sci. Instrum.* **64**, 2547.

Zhang, Q., Bahadur, D., Dufresne, E. M., Grybos, P., Kmon, P., Leheny, R. L., Maj, P., Narayanan, S., Szczygiel, R., Ramakrishnan, S. & Sandy, A. (2017). *Phys. Rev. Lett.* **119**, 178006.

Zhang, Q., Dufresne, E. M., Grybos, P., Kmon, P., Maj, P., Narayanan, S., Deptuch, G. W., Szczygiel, R. & Sandy, A. (2016). *J. Synchrotron Radiat.* **23**, 679–684.

Zhou, X. (2008). *A Practical Guide to Quantitative Finance Interviews.* CreateSpace, 14th ed. Page 88, Meeting Probability.
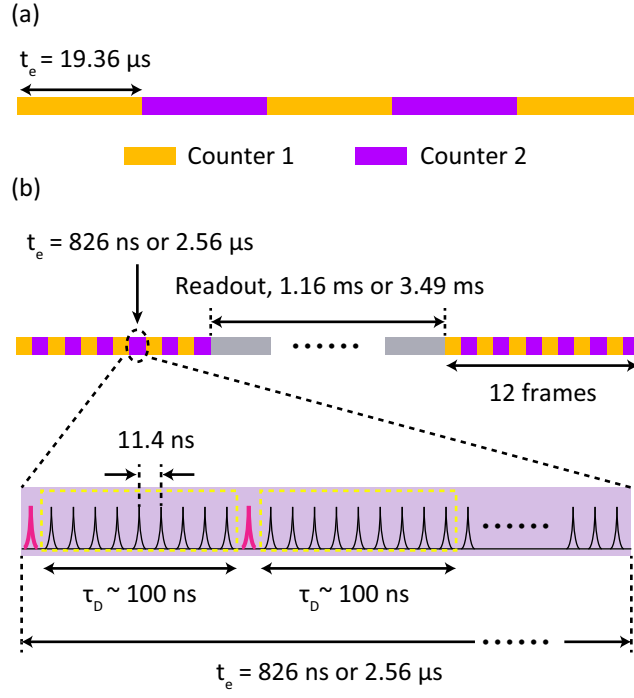
Fig. 1. Illustration of the timing structures for (a) continuous- and (b) burst-mode acquisition. In continuous mode, the two counters per pixel alternate between accumulating events and being readout. In burst mode, the counts in 12× short exposures are stored in the pixel-local counters before a longer interval is used to read out the stored data. The schematic below (b) illustrates pixel-response dead-time and its effect on recording multiple photons in a single exposure.
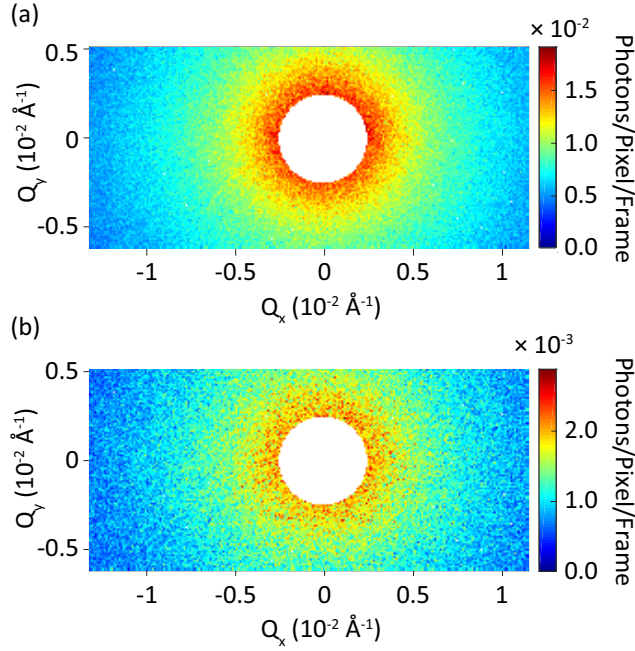
Fig. 2. Time average 2-D SAXS patterns acquired from the gold nanoparticle suspensions using (a) continuous- and (b) 2.56 μs burst-mode operation of the detector. The white circle in the center of each image is the shadow of the beam stop that has been masked out of the analysis while isolated white pixels are blemishes that have also been masked out.
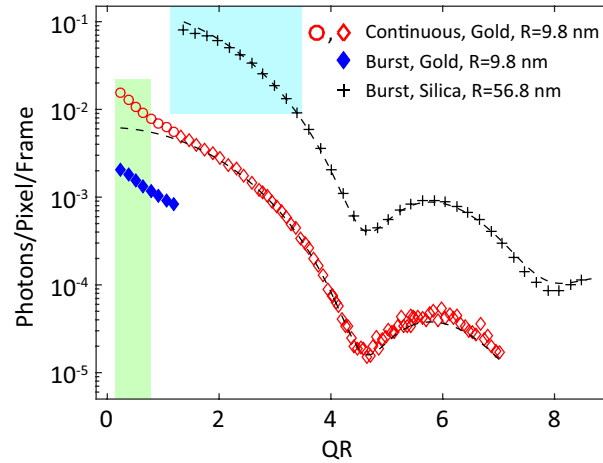
Fig. 3. SAXS intensity from continuous and 2.56 μs burst modes versus the scaled wavevector transfer QR. Dashed lines are fit results described in the text. Shaded regions indicate the ranges where the intensity autocorrelation functions displayed in Figs. 4 and 5 have been calculated.
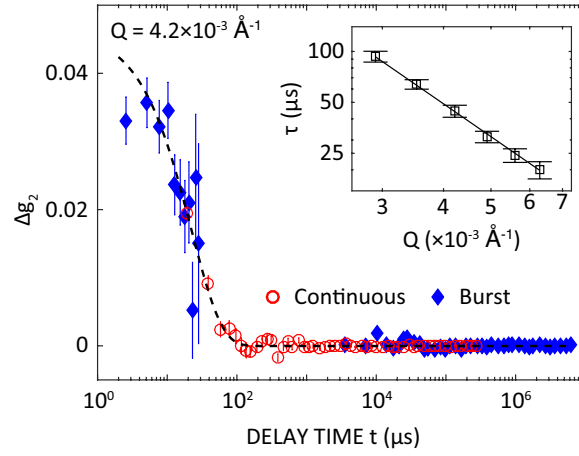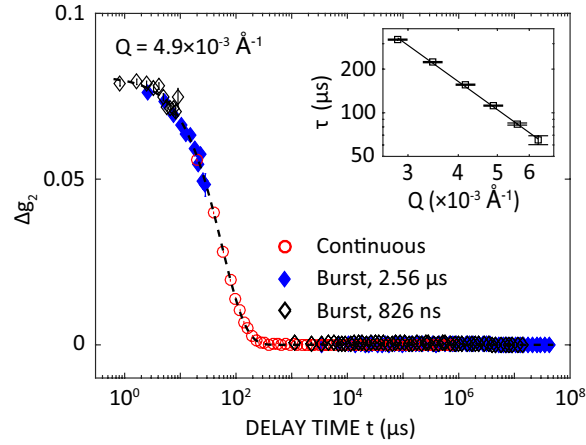
Fig. 4. Time autocorrelation determined for gold suspension hybrid-mode data. The dashed line is a fit as described in the text. The inset shows τ versus Q (open squares) and the solid line is a fit with the slope set to -2.

Fig. 5. Time autocorrelation determined for silica suspension hybrid-mode data. The dashed line is a fit as described in the text. The inset shows τ versus Q (open squares) and the solid line is a fit with the slope set to -2.
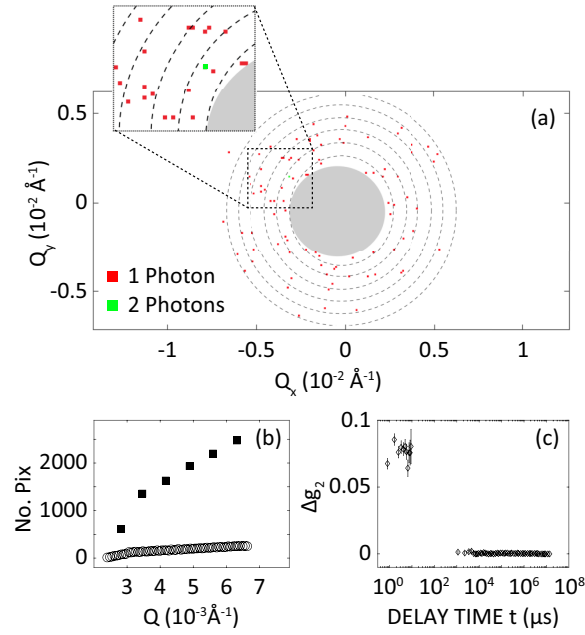
Fig. 6. 1.2 MHz burst-mode data acquired from the 57-nm-radius silica suspension. (a) A single frame showing the sparsity of the signal. (b) Number of equivalent pixels in the static (open circles) and dynamic (solid squares) partitions. (c) Δg_2 calculated from one burst-mode acquisition sequence of 180,000 frames.
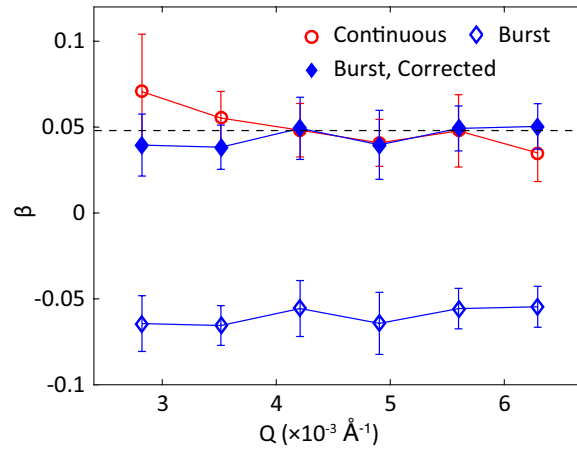

Fig. 7. β values determined by comparing the relative distribution of 1- and 2-photon events for 2.56 μs burst- (open diamonds) and continuous-mode data (open circles) acquired from the gold suspension. The solid diamonds are β values calculated after correcting for pixel-response dead-time. The dashed black line indicates $\beta = \beta_1$ obtained from a static reference sample. The error bars are estimated from the standard deviation of β in each Q bin.
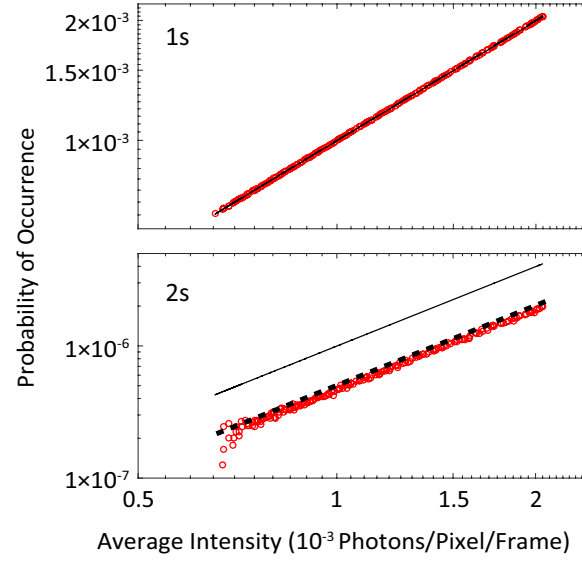
Fig. 8. 2.56 μs burst-mode measured probabilities (open symbols) for 1- and 2-photon counts (top and bottom panels, respectively) in a pixel as a function of the average intensity in a pixel. The solid and dashed lines are the calculated probabilities for fully coherent and fully incoherent (Poisson) scattering.